# Numerical Simulation of a High-Lift Configuration Embedded with High Momentum Fluidic Actuators

Veer N. Vatsa[*]

*NASA Langley Research Center, Hampton,VA 23681*

Benjamin Duda[†]

*Exa GmbH, Landshuter Allee 8, 80637 Munich, Germany*

Ehab Fares[‡]

*Exa GmbH, Curiestrasse 4, D-70563, Stuttgart, Germany*

and

John C. Lin[§]

*NASA Langley Research Center, Hampton,VA 23681*

   **Numerical simulations have been performed for a vertical tail configuration with deflected rudder. The suction surface of the main element of this configuration, just upstream of the hinge line, is embedded with an array of 32 fluidic actuators that produce oscillating sweeping jets. Such oscillating jets have been found to be very effective for flow control applications in the past. In the current paper, a high-fidelity computational fluid dynamics (CFD) code known as the PowerFLOW® code is used to simulate the entire flow field associated with this configuration, including the flow inside the actuators. A fully compressible version of the PowerFLOW® code valid for high speed flows is used for the present simulations to accurately represent the transonic flow regimes encountered in the flow field due to the actuators operating at higher mass flow (momentum) rates required to mitigate reverse flow regions on a highly-deflected rudder surface. The computed results for the surface pressure and integrated forces compare favorably with measured data. In addition, numerical solutions predict the correct trends in forces with active flow control compared to the no control case. The effect of varying the rudder deflection angle on integrated forces and surface pressures is also presented.**

[*] Senior Research Scientist, Computational AeroSciences Branch, Research Directorate; Associate Fellow AIAA

[†] Senior Application Engineer, Aerospace

[‡] Senior Technical Director, Aerospace Applications; Senior Member AIAA

[§] Senior Research Engineer, Flow Physics and Control Branch, Research Directorate; Associate Fellow AIAA

American Institute of Aeronautics and Astronautics

## Nomenclature

AFC      active flow control
$A_{nozzle}$      total exit area of all actuators
$A_{ref}$      total projected area of entire vertical stabilizer model
b      semi-span
CFD      computational fluid dynamics
$C_D$      drag coefficient, $F_x/(0.5\rho_\infty V_\infty{}^2 A_{ref})$
$C_Y$      side-force coefficient, $F_y/(0.5\rho_\infty V_\infty{}^2 A_{ref})$
$C_{Yo}$      side-force coefficient for non-actuated case
$C_\mu$      momentum coefficient, $\frac{A_{nozzle}}{2*A_{ref}} * (\frac{V_j}{V_\infty})^2$
$C_p$      pressure coefficient, $(p - p_\infty)/(0.5\rho_\infty V_\infty{}^2)$
c      chord
DNS      direct numerical simulation
exp      experimental
ERA      Environmentally Responsible Aviation
$F_x$      $x$-component of integrated force on vertical stabilizer
$F_y$      $y$-component of integrated force on vertical stabilizer
kg      kilogram
LBM      Lattice Boltzmann Model
M      Mach number
MAC      mean aerodynamic chord
m      meters
NASA      National Aeronautics and Space Administration
t      time
sec      seconds
V      total velocity
VR      variable resolution regions
3-D      three-dimensional
$u, v, w$      Cartesian fluid velocity components
$x, y, z$      Cartesian coordinates
$\delta_R$      rudder deflection angle
$\beta$      yaw angle
$\rho$      density

**Superscript:**
$^\circ$      degree

**Subscript:**
$j$      jet exit quantity
$\infty$      freestream quantity

## I.  Introduction

There has been a growing emphasis in recent years on meeting the stringent restrictions on emissions and noise imposed by regulatory agencies for commercial aircraft. A significant effort is being devoted to reduce the noise and fuel burn (emissions) through research activities at NASA in the Environmentally Responsible Aviation (ERA) project. One area of research under this project is to increase the lift/drag ratio and/or to reduce the size of control surfaces on aircraft by making use of active flow control (AFC) devices, which will decrease the overall drag, weight and fuel burn of the aircraft, and hence reduce the emissions for a given payload. The AFC devices have to be designed to maximize performance with the least amount of weight penalty and power requirements. In addition, these devices must have acceptable fault tolerance.

American Institute of Aeronautics and Astronautics

Recent advances in computational fluid dynamics (CFD) methods have made it possible to simulate the effect of AFC devices on major aircraft components, as evidenced by a series of publications in the literature.[1–5] The paper of Collis et al.[4] summarizes the various issues encountered in AFC applications from both theoretical and experimental points of view. In most of these studies, flow control was achieved primarily with synthetic or pulsed-jet actuators. These types of devices invariably consist of moving parts and controllers that increase the system complexity, which in turn can cause operational problems in flight.

Seifert[6] examined the characteristics and operational mechanisms of several different type of actuators, and suggested criteria for comparing their efficiencies. In subsequent papers, Seifert and his co-workers[7–9] demonstrated the usefulness of AFC devices for reducing separation and drag on different vehicles, and found the suction and oscillatory blowing actuators to be better suited for their applications. More recently, Shmilovich, Yadlin and Whalen[10] have examined the effect of jets blowing through a series of actuators on a vertical tail configuration to mitigate flow separation and help increase control authority of the vertical tail. The computational approach used in Ref. 10 relies on time-varying boundary conditions at the nozzle exits to simulate the excitation due to control devices.

During the last several years, fluidic actuators have been identified as viable flow control devices for improving the aerodynamic performance of high-lift configurations by mitigating separated flow regions. Such devices do not contain any moving parts and rely primarily on the feedback mechanism triggered by the unsteady flow inside the actuators. DeSalvo et al.,[11] Woszidlo and Wygnanski,[12] and Seele et al.[13] have examined the performance of such actuators for high-lift configurations. Based on the available research, the fluidic actuators that produce spanwise oscillating or sweeping jets without using any moving components, offer a reliable and efficient mechanism for AFC applications.

In a recent paper, Vatsa et al.[14] used CFD simulations to examine the internal and external flow structures created by an array of fluidic actuators embedded in a high-lift configuration resembling a vertical tail with rudder, a configuration that has been tested experimentally by Seele et al.[15] As a result of this work, the usefulness of a Lattice-Boltzmann Model (LBM) based approach available in the PowerFLOW® CFD code was demonstrated for simulating the effect of fluidic actuators on such configurations that produce large side force when the rudder is deflected. However, because of the Lattice-Boltzmann formulation available in the PowerFLOW® code at the time, we were not able to simulate fluid actuators at higher mass flow rate (momentum) that can create pockets of transonic flow in the vicinity of the actuator throat. Instead of the mass flow rate, a typical parameter used for comparing the performance and scaling of AFC actuators is the momentum coefficient ($C_\mu$), which can be defined by the expression: $C_\mu = \frac{A_{nozzle}}{2*A_{ref}} * (\frac{V_j}{V_\infty})^2$, where $A_{nozzle}$ is the exit area of the actuator, $A_{ref}$ is the planform area of the configuration, $V_j$ is the jet exit velocity, and $V_\infty$ is the freestream velocity. The actuation cases presented in this paper will be identified by their respective $C_\mu$ levels.

Fares et al.[16] have recently validated a version of the PowerFLOW® code for transonic and supersonic flows. This higher speed (transonic) version of the PowerFLOW® code is used in the current paper to repeat the simulations for the vertical tail configuration of Ref. 14, where fluidic actuators were supplied with lower mass flows to avoid transonic flow conditions. In addition, we also present cases with higher mass flow rates ($C_\mu$) to calibrate the performance of fluidic actuators operating at higher jet exit speeds in the transonic regime.

## II.   Configuration and Test Conditions

The configuration under consideration here corresponds to the vertical tail (stabilizer) model tested by Seele et al.[15] at the California Institute of Technology's Lucas Wind Tunnel,[17] shown schematically in Fig. 1. The basic section of this model has a NACA 0012 profile. The wing is tapered and has a leading edge sweep of $42°$ and a 35% chord rudder (flap). It has a span of 3.5 feet (1.067 m) and a mean aerodynamic chord (MAC) of 1.765 feet (0.538 m). We will refer to the wing section up to the hinge line as the main element, and the flap as the rudder for discussion purposes in this paper. This model has 32 fluidic actuators embedded on the suction surface of the main element distributed over the entire span such that the actuator exits are situated in front of the rudder leading edge. The fluidic actuators used on this model have internally curved geometry, and have been studied experimentally by Woszidlo and Wygnanski[12] and computationally by Vatsa et al.[18] Such internally curved actuators that produce sweeping jets were found to be more efficient for flow control applications compared to synthetic jets. Additional details of this configuration and test setup are available in Ref. 15.

The fluidic actuators were supplied with compressed air from a feed tube inserted through the root of the wind-tunnel model. The flow rate of air entering the actuators was controlled by an electronic pressure regulator connected to the feed tube. The ejected mass flow was measured by a flow meter. All 32 actuators were located near the trailing edge of the main element, just upstream of the rudder hinge line. Actuator # 1 is positioned closest to the root section, whereas actuator # 32 is placed near the wing tip. The flow exits the actuators at an angle of approximately $10°$ relative to the surface of the main element of the vertical tail and normal to the rudder hinge line pointing in the downstream direction.

The nominal freestream velocity in the tunnel is 40 m/sec. To minimize Reynolds number and transition effects for such low speed flows, trip dots were applied at $x/c = 5\%$ on the suction side and $x/c = 10\%$ on the pressure side of the model. Pressure measurements along the chordwise direction are available for this configuration at three different locations corresponding to 40, 70, and 89% span stations of the main element, as shown schematically in Fig. 2. Note that the pressure measurements for this configuration are available along lines that are normal to the leading edges of the main element and the rudder sections. Side force and drag force measurements are also available to quantify the effectiveness of the actuators as control devices for improving the performance of the vertical stabilizer.

## III.   Simulation Method

Numerical simulations presented in this paper were performed using the commercial CFD software PowerFLOW®, which is a compressible flow solver based originally on the three-dimensional 19 state (D3Q19) Lattice Boltzmann Model (LBM). The PowerFLOW® code represents LBM based CFD technology developed over the last 30 years,[19–23] and has been extensively validated for a wide variety of applications ranging from academic direct numerical simulations (DNS) cases to industrial flow problems in the fields of aerodynamics[24] and aeroacoustics.[25] In contrast to methods based on the Navier-Stokes (N-S) equations, LBM uses a simpler and more general physics formulation at the microscopic level.[19] The LBM equations recover the macroscopic hydrodynamics of the Navier-Stokes equations[26,27] through the Chapman-Enskog expansion. The local formulation of the LBM equations allows a highly efficient implementation for distributed computations on thousands of processors. The low dissipation and dispersion properties of the numerical scheme produces aerodynamic and aeroacoustic results that are generally comparable to large eddy simulations obtained with classical CFD solvers, as shown in Refs. 28 and 29, and demonstrated in the comparative study of flow over tandem cylinders by Lockard.[30]

The classical LBM scheme is typically valid in the low Mach number regime up to a Mach number of 0.4. Recent extensions of the scheme recover a fully unsteady compressible form of the Navier–Stokes equations.[16,31,32] Application of this new version at transonic conditions were presented in recent papers by Koeing and Fares[33] for the NASA common research model (CRM), and by Duda et al.[34] for a sweeping jet (fluidic) actuator operating at choked conditions. The newer version of the PowerFLOW® code, which incorporates the modified LBM scheme suitable for simulating flows containing transonic flow regimes will be referred to as the fully compressible or transonic version in this paper. All of the results presented here were obtained using the transonic version of the PowerFLOW® code.

The PowerFLOW® code can be used to solve the Lattice-Boltzmann equation in a DNS mode,[35] where all of the turbulent scales are spatially and temporally resolved. However, for most engineering problems at high Reynolds numbers, the simulations are usually conducted in conjunction with a hybrid turbulence modeling approach where the small scales are modeled and larger, energy-containing scales are directly resolved. For the current work, the Lattice-Boltzmann Very Large Eddy Simulation (LB-VLES) approach described in Refs. 21, 22 and 36 is used.

The standard Lattice-Boltzmann boundary condition for no-slip or the specular reflection for free slip condition are generalized through a volumetric formulation[19,20] near the wall for arbitrarily oriented surface elements (surfels) within the Cartesian volume elements (voxels). This formulation of the boundary condition on a curved surface cutting the Cartesian grid is automatically mass, momentum, and energy conserving, and is compatible with the general second-order spatial accuracy of the underlying LBM numerical scheme. To reduce the resolution requirement near solid surfaces for high Reynolds number flows, a hybrid wall function is used to model the near wall region of the boundary layer.[24,37]

The Lattice-Boltzmann equation is solved on embedded Cartesian meshes, which are generated automatically within the flow solver for the configuration under consideration. Variable resolution (VR) regions can be defined to allow for local mesh refinement of the grid by successive factors of two in each direction.[19] The PowerFLOW® code scales well on modern computer clusters consisting of thousands of processors, making it ideally suitable for large scale applications. The LBM methodology described here has been extensively validated for a wide variety of applications ranging from academic cases by using DNS[35] to industrial flow problems in the fields of aerodynamics, thermal management, and aeroacoustics, see e.g., Refs. 5, 24 and 37–39.

## IV.   Computational Setup

The computational setup used in the present study is shown in Fig. 3. The simulation domain is enclosed by top, bottom, and side walls where a slip boundary condition is imposed. A viscous, no-slip condition is imposed on the central patch of the bottom wind tunnel wall surrounding the wing root. The upstream size of this viscous wall patch is such that a prescribed value of the boundary layer thickness is achieved at a selected streamwise location. These

American Institute of Aeronautics and Astronautics

computational boundaries are used here to approximate the walls of the Caltech Lucas wind tunnel.[17] Note that the region below the mounting plate in the wind tunnel is ignored in current simulations.

Fig. 4 shows a global view of the actuation line used to feed compressed air into the actuators. As shown in this figure, all of the actuators are connected with a single feed pipe of rectangular cross section. A detailed view of the actuators in the tip region is also presented in this figure for illustration purpose. For the current simulations, total pressure based on experimental measurements is prescribed at the inlet section of the feed pipe, close to the root of the stabilizer to replicate the experimental setup. A viscous wall condition is imposed on all of the components that form the vertical stabilizer configuration. The presence of the trip dots at $x/c = 5\%$ and $x/c = 10\%$ on the suction and pressure sides of the main element is modeled by prescribing laminar patches.

Velocity is imposed at the inlet boundary, whereas static pressure is imposed at the exit boundary. The cross section of the computational domain is nearly identical to the Caltech Lucas wind tunnel. The computational domain shown in Fig. 3 is split into a total of 11 Variable Resolution (VR) levels for simulations with active flow control. The two finest VR levels are used to model the high gradient flow regions inside the actuators. In the no-control case, the overall number of VR levels is reduced to 9 by coarsening the resolution in the actuator nozzles. The minimum voxel (cubic cell) edge length is 3.39 x $10^{-5}$ m and 1.35 x $10^{-4}$ m for the control and no-control cases, respectively. In the actuated (control) case, 30 grid cells are used along the shortest dimension of any rectangular sectional area along the actuator axis. The coarsest voxel size anywhere in the computational domain is set at 0.035 m for all the cases. More detailed information regarding the computational setup of this configuration is available in Ref. 14.

The PowerFLOW® code uses explicit time marching to solve the governing equations in a time consistent manner. The time step used for advancing the solutions is based on stability considerations. The solution on a given VR level is updated twice as often when compared to the number of solution updates on the next coarser VR level. Thus, the solution on the finest grid is updated most frequently, whereas the solution on the coarsest grid is updated least often to advance the solution in the whole domain to the same physical time. A comparable number of voxels (cells) on coarser grids are therefore less expensive from the computational point of view.

## V.   Results

The computations of the three-dimensional (3-D) flow field for the vertical stabilizer configuration with and without flow control (actuation) have been performed using the transonic version of the PowerFLOW® code. The baseline conditions chosen for this work correspond to zero mass flow (no actuation) at a freestream speed of 40 m/sec and a rudder deflection of $30°$. The Reynolds number based on the mean aerodynamic chord is 1.36 million. In addition to the no-actuation case ($C_\mu = 0$), the experimental data for this configuration is also available for several other values of momentum coefficient. Computational results are presented for rudder deflection angles of 30 and $40°$ at $C_\mu = 0$, 0.5, 1.0, and 1.5%, corresponding to the experimental study of Seele et al.[15]

The geometric manipulation and grid generation capability available in the PowerFLOW® software makes it very convenient to conduct parametric studies for complex configurations. For the current configuration, the main element and rudder geometries are imported as individual surfaces. With the available information about the center and axis of rotation, we can easily change the rudder deflection ($\delta_R$) and yaw ($\beta$) angles to match the experimental test conditions. In addition, the grid resolution is easily changed via input parameters and the grids are generated automatically by the software. Effect of yaw is not addressed in this paper, and all the results presented here correspond to $\beta = 0°$.

### V.A.   Baseline Configuration, $\delta_R = 30°, \beta = 0°$

The baseline configuration considered for this study is the vertical tail configuration of Seele et al.[15] with a rudder deflection angle ($\delta_R$) of $30°$, and a yaw angle ($\beta$) of $0°$. For no actuation case ($C_\mu = 0$) at these geometrical settings, a grid consisting of 440 million voxels distributed among 9 VR regions was used. For the actuated cases ($C_\mu = 0.5, 1.0$ and $1.5\%$ ), the computational mesh employed two additional VR regions for a total of 11 VR regions resulting in 642 million voxels. Because the finest cell size and time step for the actuated case was $\frac{1}{4}$th compared to the non-actuated case, greater number of time steps were required for the flow field to settle for the actuated case, resulting in higher computational cost for such cases.

In the current approach, the unsteady flow developing inside the fluidic actuators is computed with the PowerFLOW® CFD code for the actuated cases, instead of using approximate surface boundary conditions to simulate the effect of actuators on the external flow. As observed in Ref. 18, the jet exit velocity and frequency of spanwise oscillations of the exit flow depend primarily on the input mass flow (or gauge pressure) and the geometric details of the actuators. The total mass flow going through the actuators is 0.01433 kg/sec for $C_\mu = 0.5\%$, 0.02027 kg/sec for $C_\mu = 1.0\%$, and 0.02485 kg/sec for $C_\mu = 1.5\%$, respectively.

American Institute of Aeronautics and Astronautics

The computations are run long enough for the integrated forces to start settling in time before extracting the surface data. Typical convergence histories of the drag ($C_D$), and side force ($C_Y$) coefficients for non-actuated and actuated cases are shown in Fig. 5. Note that due to the inherent unsteady nature of the flow associated with such configurations, the force coefficients display low level of oscillations even for the non-actuated case after the initial transients are settled. A higher level of oscillations in the force coefficients is observed for the corresponding actuated cases due to the presence of bi-stable unsteady flow inside the fluidic actuators. The computed values of side force ($C_Y$) coefficients are compared with the experimental data of Ref. 15 in Table 1. The simulations predict the correct qualitative trends with actuation, although the increment in side force due to actuation is underpredicted for lower values of $C_\mu$.

**Table 1. Comparison of force coefficients, $\delta_R = 30°$.**

| $\delta_R(deg)$ | $\beta(deg)$ | $C_\mu(\%)$ | $C_Y$ (exp) | $C_Y$ (CFD) | $[C_Y\text{-}C_{Y_0}]$ (exp) | $[C_Y\text{-}C_{Y_0}]$ (CFD) |
|---|---|---|---|---|---|---|
| 30.0 | 0.0 | 0.0 | 0.780 | 0.893 | 0.000 | 0.000 |
| 30.0 | 0.0 | 0.5 | 0.919 | 0.961 | 0.139 | 0.068 |
| 30.0 | 0.0 | 1.0 | 1.067 | 1.158 | 0.287 | 0.265 |
| 30.0 | 0.0 | 1.5 | 1.163 | 1.280 | 0.383 | 0.387 |

The computed chordwise time-averaged pressure distributions at three spanwise stations, namely the inboard (40%), middle (70%) and outboard (89%) stations (see Fig. 2 for schematic of span locations), are presented in Fig. 6 for $C_\mu$ = 0.0, 1.0 and 1.5 %, respectively. Results for the $C_\mu = 0.5\%$ case closely replicate the results that were presented in a previous paper (see Ref. 14), and hence not included in these figures to avoid overcrowding. The experimental data corresponding to these test conditions is also shown in this figure. The agreement between the computed and measured pressure distributions for the non-actuated case is quite good, except for the suction surface of the rudder at the inboard station. There was some uncertainty regarding the precise details of a model mounting plate that produced a small offset at the root of the model, and formed a small gap between the rudder side edge at the root and the wind tunnel floor with rudder deflection. This is precisely the region where the computed results differ the most from the measured data in Fig. 6.

The pressure distributions obtained for the actuated ($C_\mu = 1.0\%$ and 1.5%) cases indicate higher suction pressure levels due to injection of higher momentum fluid from the actuators over the rudder leading edge, and the computational results are found to be in good agreement with the measurements over most of the main wing section. The predicted suction peak levels are in good agreement with the experimental data over most of the suction surface, but occur slightly downstream of the hinge line compared to the measurements. Such discrepancy could be attributed to either slight differences in geometry or lack of resolution in the suction surface gap region along the hinge line. Despite these differences, the computed results display the correct overall trends in pressure distribution with active flow control using fluidic actuators. In particular, the computed $C_p$ distributions for the actuated cases are found to be in excellent agreement with the measured data on most of the suction surface of the rudder and reproduce the experimentally-observed pressure recovery at the trailing edge for these actuation levels. Such pressure recovery is indicative of the flow on the rudder becoming fully attached at $C_\mu = 1.0$ and 1.5%. This in turn results in a higher value of side force coefficient, as shown in Table 1.

Simulated surface streamline patterns for this configuration at different actuation levels are presented in Fig. 7. Pressure contours are also superimposed in these figures. These pressure contours indicate higher acceleration (velocity) levels in the leading edge region of the rudder for an increased level of actuation. The biggest difference in streamline pattern for these cases is observed downstream of the hinge line of the rudder. A well defined attachment line delineating the reverse flow region is visible for the $C_\mu = 0$ (no actuation), and $C_\mu = 0.5\%$ cases on the rudder. For the $C_\mu = 1.0\%$ case, the flow on the rudder surface appears to be mostly attached with a slight flow inclination toward the tip region. By contrast, the reverse flow on the rudder disappears completely for the $C_\mu = 1.5\%$ case, and the streamlines are aligned with the streamwise direction.

Although, the footprint of a corner vortex can be seen in Fig. 7 for $C_\mu = 0.0$ and 0.5, a better view of the vortical flow under these conditions is observed in Fig. 8, where unconstrained (volumetric) streamlines are presented. Identical seeding near the corner juncture and the tip regions are used for generating the streamline pattern for all of these cases. A well-defined vortex is formed at the juncture region that propagates towards the tip region for the $C_\mu = 0$ and $0.5\%$ cases. Only a slight hint of a corner vortex is visible for $C_\mu = 1.0\%$; and it is totally missing for the actuation level of $C_\mu = 1.5\%$, which is fully attached on the rudder. As expected, a tip vortex is present for all of these actuation levels. Based on these results, it appears that an actuation level of $C_\mu = 1.5\%$ is required to fully mitigate the reverse flow for a rudder deflection of 30°; although for all practical purposes, the reverse flow is nonexistent even at $C_\mu = 1.0\%$.

American Institute of Aeronautics and Astronautics

## V.B.   Higher Rudder Deflection Configuration, $\delta_R = 40°, \beta = 0°$

The next configuration under consideration had a value of $\delta_R = 40°$ for the rudder deflection angle. The process of setting up this case with increased rudder deflection angle was very straightforward and required changing just one parameter in the PowerFLOW® case setup of the baseline configuration. Simulations have been performed with these rudder angle settings at $C_\mu = 0.0$, 0.5, 1.0 and 1.5%, which correspond to the actuation levels that were used for the baseline ($\delta_R = 30°$) configuration. Once again, the simulations were run long enough in time for the overall flow and integrated forces to settle down before extracting the time-averaged flow quantities.

The computed values of side force ($C_Y$) coefficients based on these simulations are compared with the experimental data of Ref. 15 in Table 2. The simulations predict the correct qualitative trends with actuation, although the increment in side force due to actuation is underpredicted for lower values of $C_\mu$. This trend is similar to the lower rudder deflection case that was presented in the previous subsection.

**Table 2.  Comparison of force coefficients, $\delta_R = 40°$.**

| $\delta_R(deg)$ | $\beta(deg)$ | $C_\mu(\%)$ | $C_Y$ (exp) | $C_Y$ (CFD) | $[C_Y\text{-}C_{Y_0}]$ (exp) | $[C_Y\text{-}C_{Y_0}]$ (CFD) |
|---|---|---|---|---|---|---|
| 40.0 | 0.0 | 0.0 | 0.918 | 1.0589 | 0.000 | 0.0000 |
| 40.0 | 0.0 | 0.5 | 0.983 | 1.0965 | 0.065 | 0.0376 |
| 40.0 | 0.0 | 1.0 | 1.065 | 1.1494 | 0.147 | 0.0905 |
| 40.0 | 0.0 | 1.5 | 1.184 | 1.3650 | 0.266 | 0.3046 |

The computed chordwise time-averaged pressure distributions extracted from the simulations are compared with the experimental data at the inboard (40%), middle (70%) and outboard (89%) stations in Fig. 9 for $C_\mu = 0.0$, 1.0 and 1.5%. The computed pressures for this case at $C_\mu = 0.5\%$ were found to be nearly identical to the results that were presented in a previous paper (see Ref. 14), and are not included in these figures. The agreement between the computed and measured pressure distributions for the non-actuated ($C_\mu = 0.0$) case, and for the $C_\mu = 1.0$ and 1.5% cases is quite good. However, the simulated results appear to overpredict the effect of actuation at $C_\mu = 1.5\%$, as observed by the higher suction pressure levels over the entire suction surface. In particular, higher suction peaks are seen aft of the hinge line. Compared to the measured data, a stronger pressure recovery at the trailing edge is also observed for this case. At the present time, the cause of this discrepancy is not clear and requires further investigation.

Simulated surface streamline patterns for this configuration at different actuation levels are presented in Fig. 10. Pressure contours are also superimposed in these figures, which indicate higher acceleration (velocity) levels in the leading edge region of the rudder for an increased level of actuation, similar to the $\delta_R = 30°$ case. The biggest difference in streamline pattern for these cases is observed downstream of the hinge line of the rudder. A well defined attachment line delineating the reverse flow region is visible for $C_\mu = 0$ (no actuation), and $C_\mu$ of 0.5 and 1% for this configuration. For the $C_\mu = 1.5\%$ case, it is difficult to identify an attachment line and a distinct zone of reverse flow. Instead, the streamlines are aligned with the spanwise direction, indicating a strong spanwise flow towards the tip region. Once again, a three-dimensional view of the unconstrained streamlines, shown in Fig. 11, provides a better perspective of the flow over the rudder. Much stronger and extensive reverse flow is observed for this higher rudder deflection angle compared to the baseline deflection angle of 30 degrees. The corner vortex is much stronger and extends further away from the surface, and is observed even at $C_\mu = 1.0\%$ over the entire span. This is consistent with the surface streamline pattern, thus confirming the existence of a significant reverse flow region at this actuation level. The corner vortex finally weakens at $C_\mu = 1.5\%$ level, although there is still a hint of reverse flow on the rudder. Based on these results, it is clear that a higher level of actuation ($C_\mu > 1.5\%$) would be required for complete mitigation of reverse flow at a rudder deflection angle of $40°$, in contrast with the baseline configuration ($\delta_R = 30°$) discussed in the previous subsection. A better flow control strategy might be to move the actuation line slightly downstream of the rudder leading edge for higher rudder deflections.

## V.C.   Flow Structure Inside Fluidic Actuators

To get a better understanding of the flow structure developing inside the fluidic actuators and its impact on the control surface, an instantaneous view of the Mach number distribution for one of the actuators for the $\delta_R = 40°$ configuration at $C_\mu = 1.5\%$, is presented in Fig. 12. The micro jets issued from the actuator nozzle can be seen merging with the external flow over the rudder downstream of the actuator nozzle exit. These figures were generated using the instantaneous flow field at two different instances in time to demonstrate the sweeping (oscillating) nature of such micro jets. The Mach number contours shown here clearly indicate the existence of sonic flow at the nozzle throat. The transonic flow is also

observed inside the micro jet cores downstream of the nozzle throat. The flow exiting the nozzle in Fig. 12 (a) is leaning to the right, whereas the flow at a later time ( Fig. 12 (b)) is leaning the other way, which is indicative of the oscillating nature of these micro jets. The ability of the fluidic actuators to produce spanwise sweeping jets that can energize much larger regions compared to straight jets issuing from the same nozzles is believed to result in higher efficiency of these devices for flow control applications per unit input mass flow. This assertion has been verified by the experimental work of Seele et al.[13,15]

## VI.   Concluding Remarks

Computational results based on numerical simulations performed using a fully compressible Lattice-Boltzmann formulation in the PowerFLOW® CFD code, which has recently been validated for transonic and supersonic flow regimes, are presented here for a vertical tail configuration with deflected rudder. This configuration has an array of fluidic actuators embedded on the suction surface of the main element in proximity of the trailing edge, just upstream of the rudder hinge line. Such actuators have been found to be very effective for flow control applications in the past. In the current approach, the entire flow field associated with this configuration, including the flow inside the actuators is simulated. The resulting solutions for force coefficients and surface pressure distributions are compared with available experimental data in the presence of actuation. Reasonably good agreement is obtained with the measured data for this configuration at rudder deflection angles ($\delta_R$) of 30 and 40 degrees, and simulated results predict the correct qualitative trends in forces with active flow control at these settings.

The newly-available, fully compressible, transonic version of the PowerFLOW® code makes it feasible to simulate actuators supplied with higher mass flow rates that result in pockets of transonic flow inside the actuators and in the vicinity of actuator throats. Results obtained with this code are presented here for mass flow rates of up to 0.02485 kg/sec ($C_\mu = 1.5\%$). Local transonic flow is observed in the vicinity of actuator throats at such high mass flow rates. The results obtained so far are very encouraging and computed surface pressures and side forces indicate the correct trends with actuation. Streamline patterns clearly illustrate reduction in reverse flow region over the rudder surface when sufficient level of actuation is applied.

## Acknowledgments

## References

[1] Shmilovich, A. and Yadin, Y., "Flow Control for the Systematic Buildup of High-Lift Systems," *Journal of Aircraft*, Vol. 45, No. 5, September-October 2008, pp. 1680–1688.

[2] Shmilovich, A. and Yadin, Y., "Flow Control Techniques for Transport Aircraft," *AIAA Journal*, Vol. 49, No. 3, March 2011, pp. 489–502.

[3] Rumsey, C., Gatski, T., Sellers III, W., Vatsa, V., and Viken, S., "Summary of the 2004 Computational Fluid Dynamics Validation Workshop on Synthetic Jets," *AIAA Journal*, Vol. 44, No. 2, 2006, pp. 194–207.

[4] Collis, S., Joslin, R., Seifert, A., and Theofilis, V., "Issues in Active Flow Control: Theory, Control, Simulation and Experiment," *Progress in Aerospace Sciences*, Vol. 40, No. 4-5, 2004, pp. 237–289.

[5] Brès, G., Fares, E., Williams, D., and Colonius, T., "Numerical Simulations of the Transient Flow Response of a 3D, Low-Aspect-Ratio Wing to Pulsed Actuation," AIAA Paper 2011-3440, June 2011.

[6] Seifert, A., "Closed-loop Active flow control systems: Actuators," *Notes on Numerical Fluid Mechanics and Multidisciplinary Design (NNFM)*, Vol. 95, 2007, pp. 85–102.

[7] Seifert, A., Stalnov, O., Sperber, D., Arwatz, G., Palei, V., David, S., Dayan, I., and Fono, I., "Large Trucks Drag Reduction Using Active Flow Control," AIAA Paper 2008-0743, January 2008.

[8] Arwatz, G., Fono, I., and Seifert, A., "Suction and Oscillatory Blowing Actuator Modeling and Validation," *AIAA J.*, Vol. 40, No. 5, 2008, pp. 1007–1017.

[9] Wilson, J., Schatzman, D., Arad, E., Shtendel, T., and Seifert, A., "Active Separation Control Appled to an Axis-symmetric Body," AIAA Paper 2012-0072, January 2012.

[10] Shmilovich, A. and Yadlin, Y. aand Whalen, E., "Computational Evaluation of Flow Control for Enhanced Control Authority of a Vertical Tail," AIAA Paper 2015-3311, June 2015.

[11] DeSalvo, M., Whalen, E., and Glezer, A., "High-Lift Enhancement using Fluidic Actuation," AIAA Paper 2010-0863, January 2010.

[12] Woszidlo, R. and Wygnanski, I., "Parameters Governing Separation Control with Sweeping Jet Actuators," AIAA Paper 2011-3172, June 2011.

[13] Seele, R., Graff, E., Gharib, M., Taubert, L., Lin, J., and Wygnanski, I., "Improving Rudder Effectiveness with Sweeping Jet Actuators," AIAA Paper 2012-3244, June 2012.

[14] Vatsa, V., Casalino, D., Lin, J., and Appelbaum, J., "Numerical Simulation of a High-Lift Configuration with Embedded Fluidic Actuators," AIAA Paper 2014-2142, June 2014.

[15]Seele, R., Graff, E., Lin, J., and Wygnanski, I., "Performance Enhancement of a Vertical Tail Model with Sweeping Jet Actuators," AIAA Paper 2013-0411, January 2013.

[16]Fares, E., Wessels, M., Li, Y., Gopalakrishnan, P., Zhang, R., Sun, C., Gopalaswamy, N., Roberts, P., Hoch, J., and Chen, H., "Validation of a Lattice Boltzmann Approach for Transonic and Supersonic Simulations," AIAA Paper 2014-0952, January 2014.

[17]http://windtunnel.caltech.edu, last accessed, March 2014.

[18]Vatsa, V., Koklu, M., Wygnanski, I., and Fares, E., "Numerical Simulation of Fluidic Actuators for Flow Control Applications," AIAA Paper 2012-3239, June 2011.

[19]Chen, H., "Volumetric Formulation of the Lattice Boltzmann Method for Fluid Dynamics: Basic Concept," *Physical Review A*, Vol. 58, September 1998, pp. 3955–3963.

[20]Chen, H., Teixeira, C., and Molvig, K., "Realization of Fluid Boundary Conditions via Discrete Boltzmann Dynamics," *Intl. J. Mod. phys. C*, Vol. 9, No. 8, 1998, pp. 1281.

[21]Yakhot, V. and Orszag, S., "Renormalization Group Analysis of Turbulence. I. Basic Theory," *J. Sci. Comput.*, Vol. 1, No. 2, 1986, pp. 3–51.

[22]Chen, H., Kandasamy, S., Orszag, S., Shock, R., Succi, S., and Yakhot, V., "Extended Boltzmann Kinetic Equation for Turbulent Flows," *Science*, Vol. 301, No. 5633, 2003, pp. 633–636.

[23]Chen, S. and Doolen, G., "Lattice Boltzmann Method for Fluid Flows," *Ann. Rev. Fluid Mech.*, Vol. 30, January 1998, pp. 329–364.

[24]Fares, E. and Nölting, S., "Unsteady Flow Simulation of a High-Lift Configuration using a Lattice Boltzmann Approach," AIAA Paper 2011-869, January 2011.

[25]Khorrami, M., Fares, E., and Casalino, D., "Towards Full-Aircraft Airframe Noise Prediction: Lattice-Boltzmann Simulations," AIAA Paper 2014-2481, June 2014.

[26]Chen, H., Chen, S., and Matthaeus, W., "Recovery of the Navier-Stokes Equations Using a Lattice-gas Boltzmann Method," *Physical Review A*, Vol. 45, 1992, pp. 5339–5342.

[27]Qiana, Y. H., D'Humiéres, D., and Lallemand, P., "Lattice BGK Models for Navier-Stokes Equations," *Europhysics Letters*, Vol. 17, 1992, pp. 479–484.

[28]Marié, S., Ricot, D., and Sagaut, P., "Comparison between Lattice Boltzmann Method and Navier-Stokes High Order Schemes for Computational Aeroacoustics," *J. of Computational Physics*, Vol. 228, 2009, pp. 1056–1070.

[29]Brès, G., Pérot, F., and Freed, D., "Properties of the Lattice-Boltzmann Method for Acoustics," AIAA Paper 2009-3395, May 2009.

[30]Lockard, D., "Summary of the Tandem Cylinder Solutions from the Benchmark problems for Airframe Noise Computations-I Workshop," AIAA Paper 2011-353, Jan. 2011.

[31]Shan, X., Yuvan, X.-F., and Chen, H., "Kinetic Theory Representation of Hydrodynamics: a Way Beyond the Navier-Stokes Equation," *Physics. Rev. Lett.*, Vol. 80, 1998, pp. 65–88.

[32]Zhuo, C., Zhong, C., Li, K., Xiong, S., Chen, X., and Cao, J., "Application of Lattice Boltzmann Method to Simulation of Compressible Turbulent Flow," *Commun. Comput. Physics*, Vol. 8, 2010, pp. 1208–1223.

[33]Koeing, B. and Fares, E., "Validation of a Transonic Lattice-Boltzmann Method for the NASA Common Research Model," AIAA Paper 2016-2023, January 2016.

[34]Duda, B., Fares, E., Wessels, M., and Vatsa, V., "Unsteady Flow Simulation of a Sweepig Jet Actuator Using a Lattice-Boltzmann Method," AIAA Paper 2016-1818, January 2016.

[35]Li, Y., Shock, R., and Chen, H., "Numerical Study of Flow Past an Impulsively Started Cylinder by Lattice Botzmann Method," *J. Fluid Mech.*, Vol. 519, November 2004, pp. 273–300.

[36]Chen, H., Orszag, S., Staroselsky, I., and Succi, S., "Expanded Analogy between Boltzmann Kinetic Theory of Fluid and Turbulence," *J. Fluid Mech.*, Vol. 519, November 2004, pp. 301–314.

[37]Fares, E., "Unsteady Flow Simulation of the Ahmed Reference Body using a Lattice Boltzmann Approach," *Comput. Fluids*, Vol. 35, No. 8-9, 2006, pp. 940–950.

[38]Brès, G., Freed, D., Wessels, M., Nöelting, M., and Pérot, F., "Flow and Noise Predictions for Tandem Cylinder Aeroacoustic Benchmark," *Physics of Fluids*, Vol. 24, No. 3, March 2012, http://dx.doi.org/10.1063/1.3685102.

[39]Casalino, D., Ribeiro, A., and Fares, E., "Facing Rim Cavities Fluctuation Modes," *Journal of Sound and Vibration*, Vol. 333, No. 13, 2014, pp. 2812–2830.

American Institute of Aeronautics and Astronautics
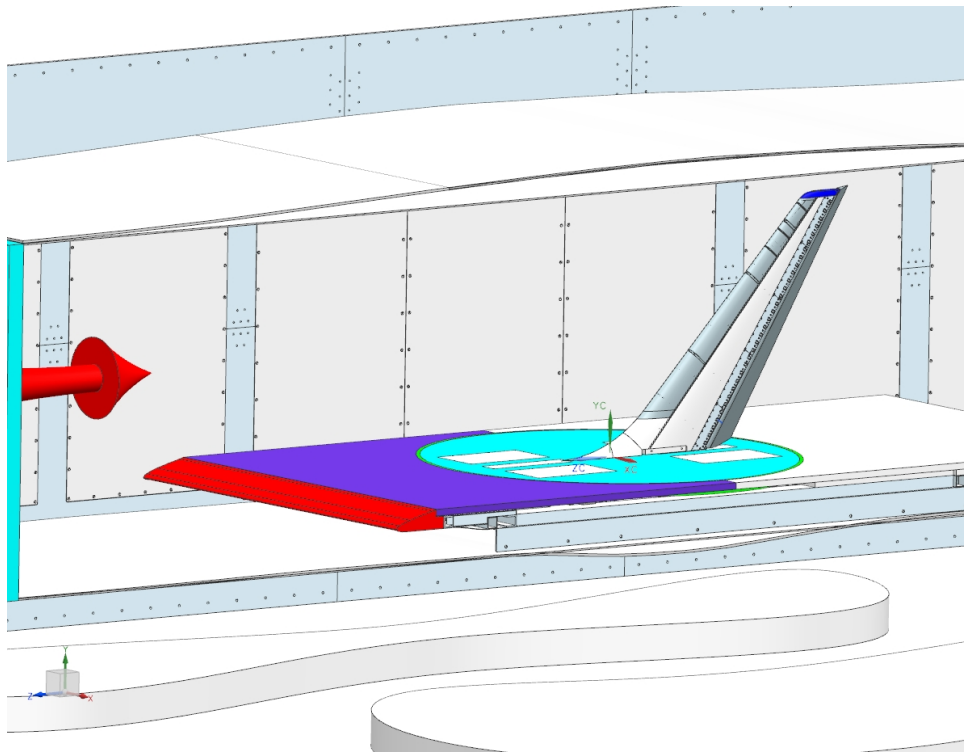
**Figure 1. Vertical tail setup in Caltech Lucas wind tunnel.**
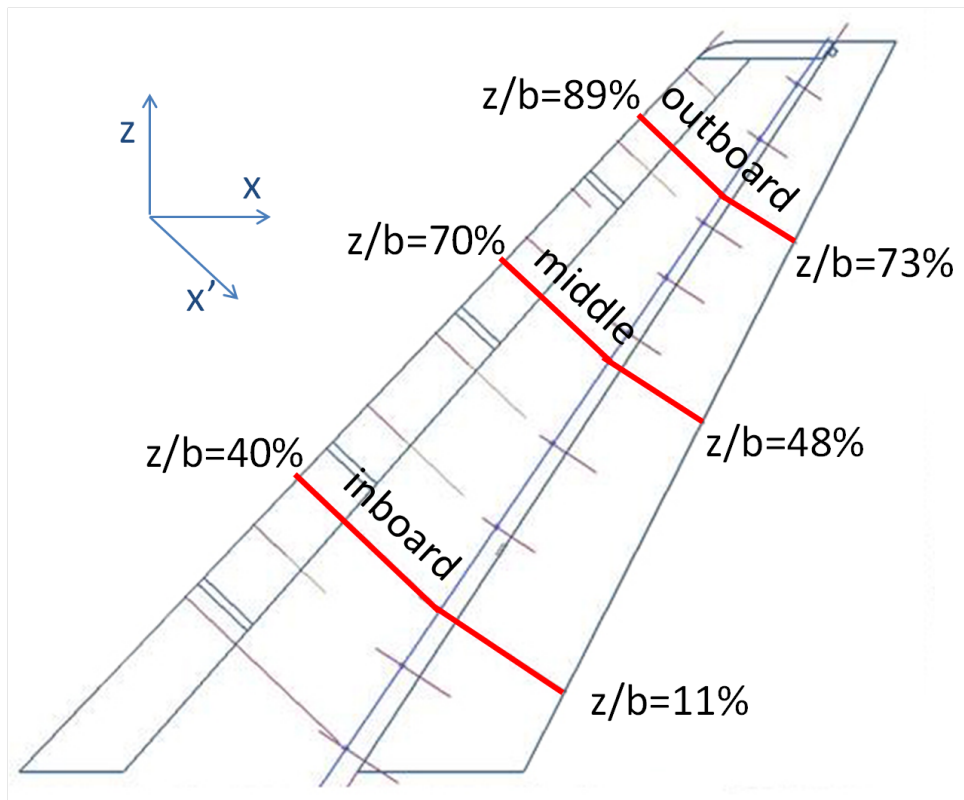


**Figure 2. Schematic of chordwise pressure tap rows.**
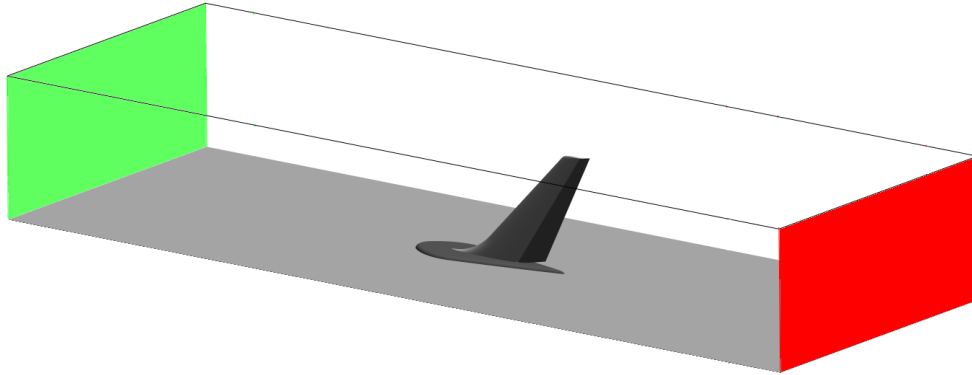
**Figure 3. Computational setup.**



**Figure 4. Actuator setup.**

American Institute of Aeronautics and Astronautics

**(a)** $C_\mu = 0.0\%$

**(b)** $C_\mu = 1.0\%$
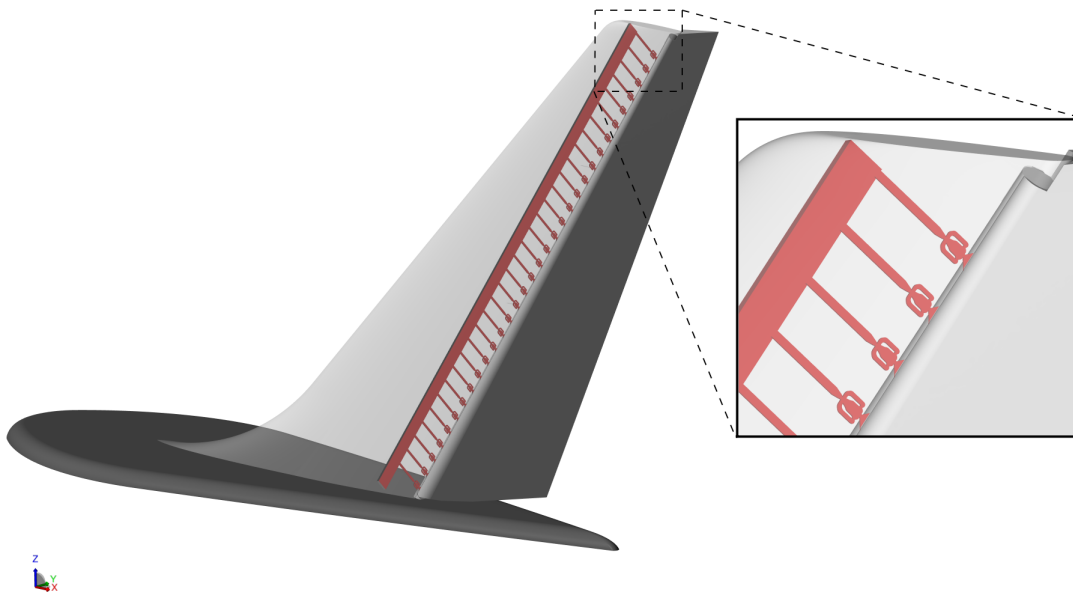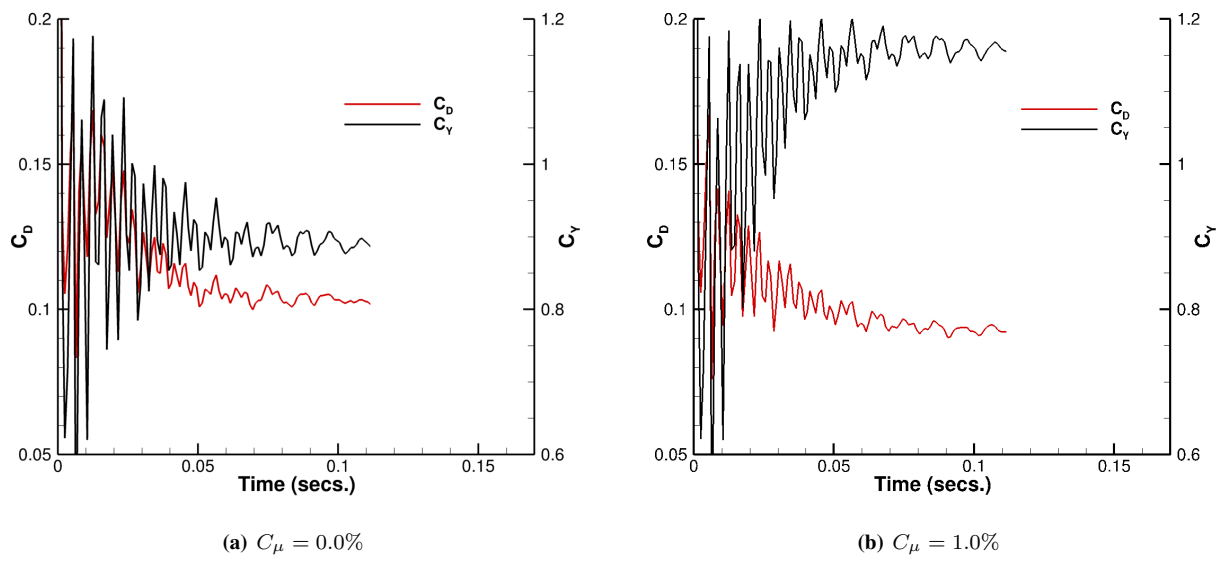
**Figure 5. Convergence history of force coefficients for baseline case.**

American Institute of Aeronautics and Astronautics
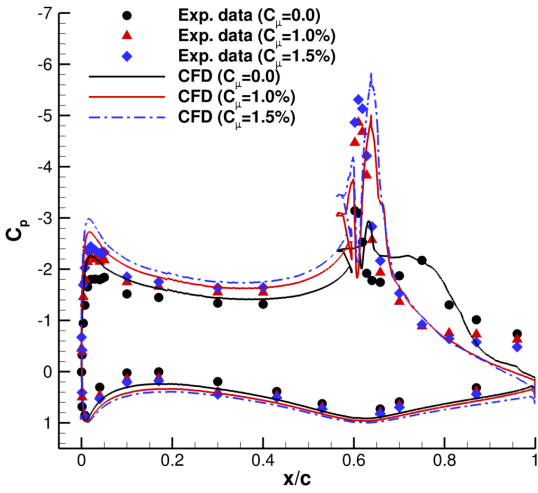
(a) inboard, $z/b = 40\%$
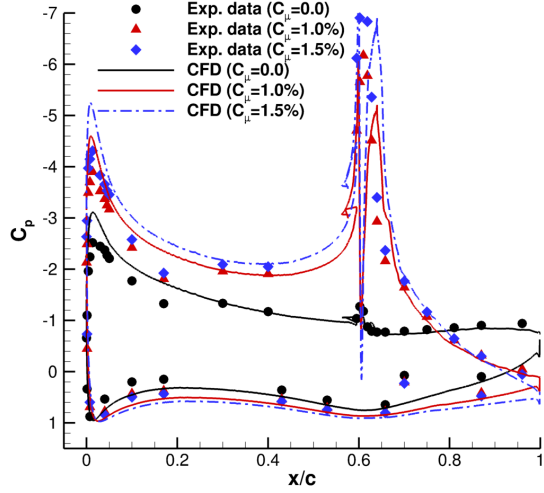


(b) middle, $z/b = 70\%$
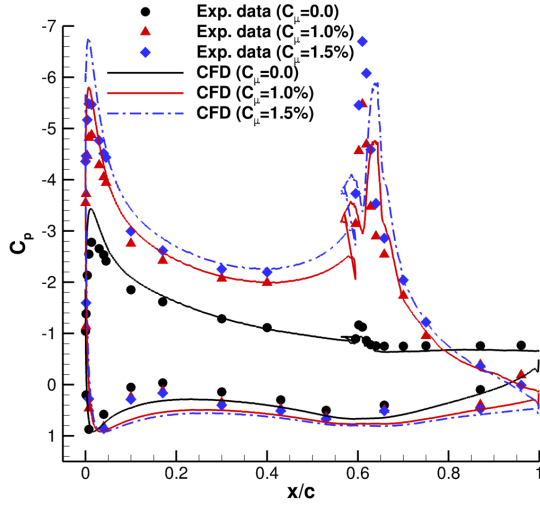


(c) outboard, $z/b = 89\%$

Figure 6. Chordwise surface pressure comparisons: baseline case, $\delta_R = 30°$, $\beta = 0°$.

American Institute of Aeronautics and Astronautics
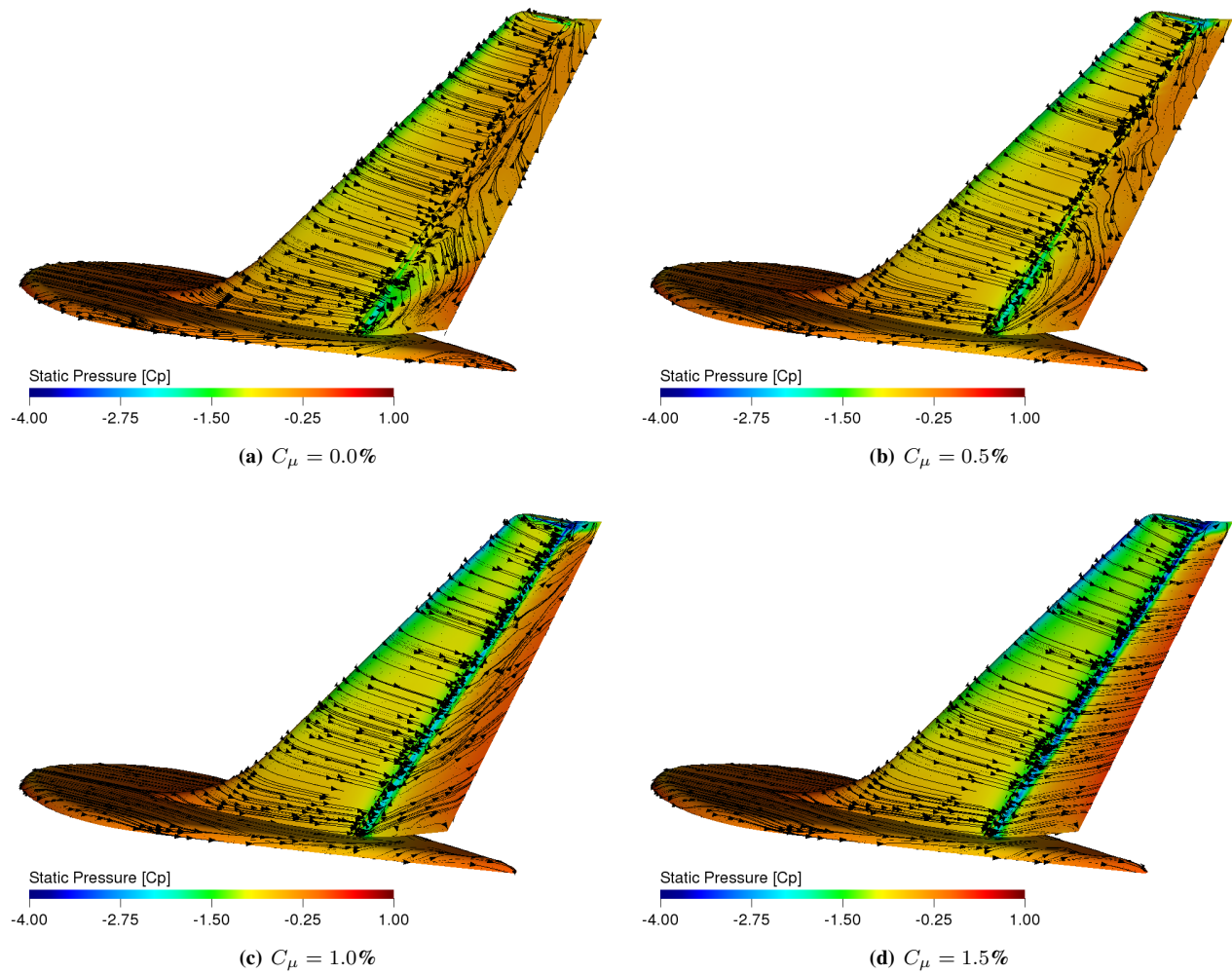
(a) $C_\mu = 0.0\%$



(b) $C_\mu = 0.5\%$



(c) $C_\mu = 1.0\%$



(d) $C_\mu = 1.5\%$

Figure 7.  Effect of actuation levels on simulated surface streamline patterns, $\delta_R = 30°, \beta = 0°$.
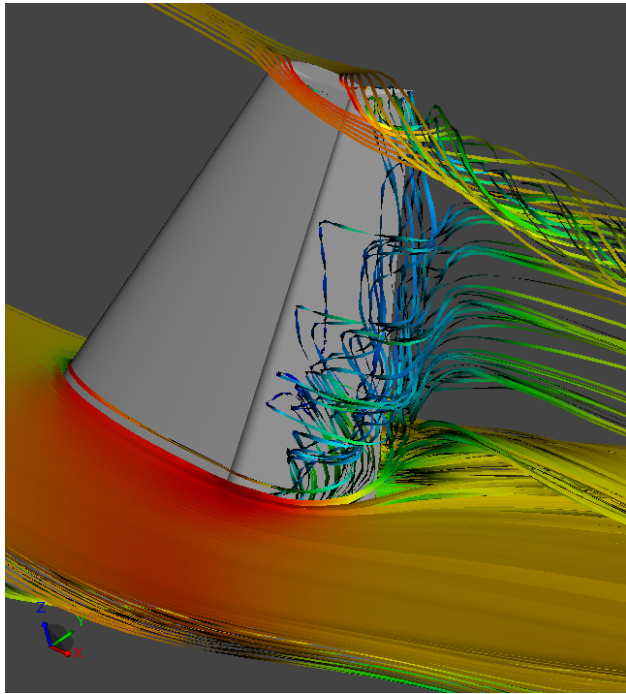
**(a)** $C_\mu = 0.0\%$
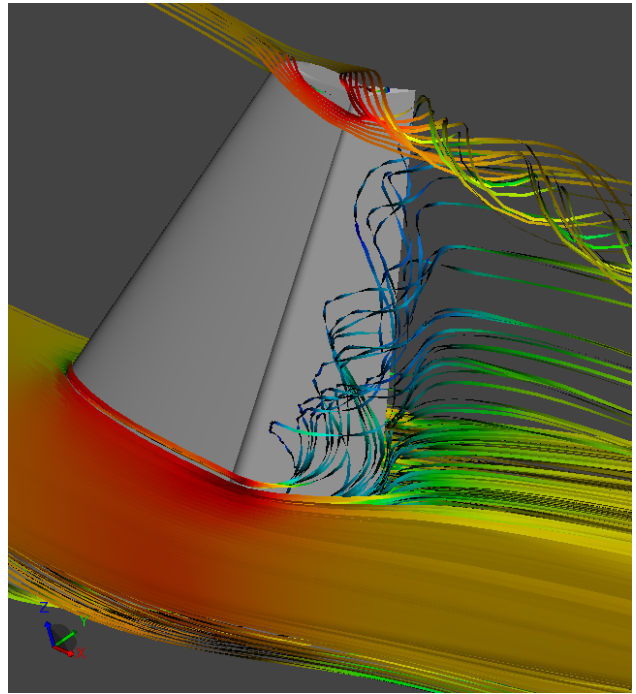
**(b)** $C_\mu = 0.5\%$
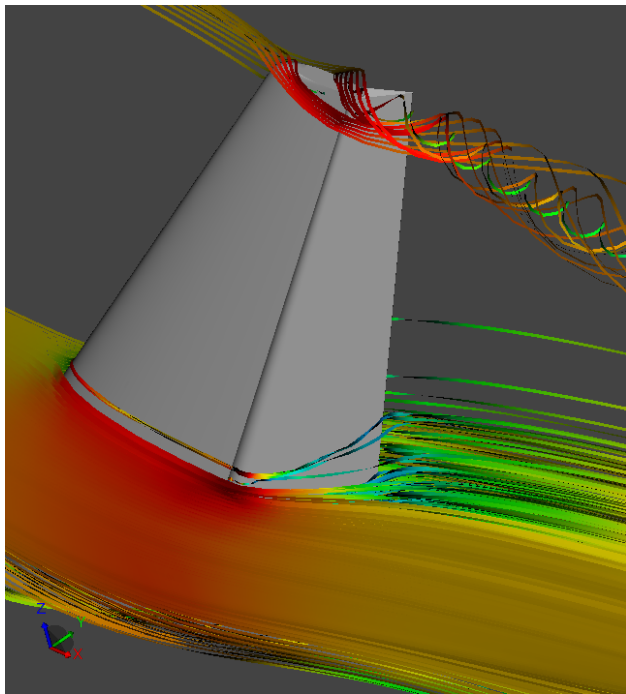
**(c)** $C_\mu = 1.0\%$
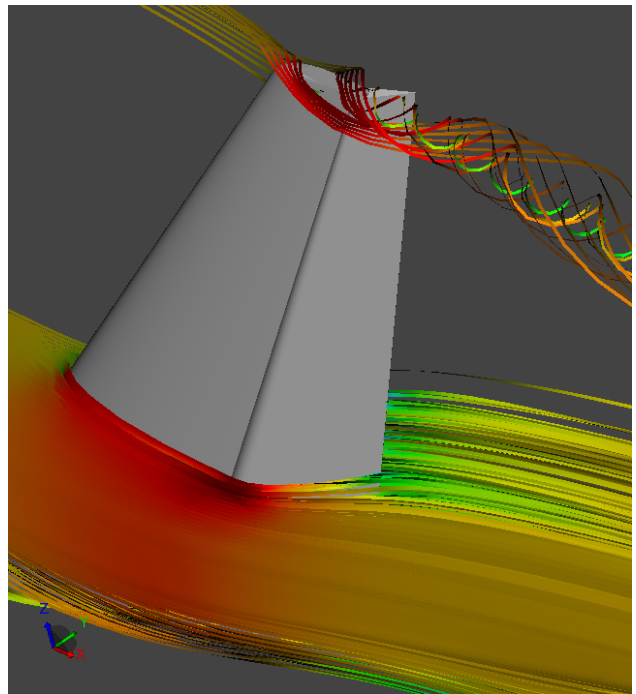
**(d)** $C_\mu = 1.5\%$

**Figure 8. Effect of actuation levels on simulated off-surface streamlines, $\delta_R = 30°$, $\beta = 0°$.**
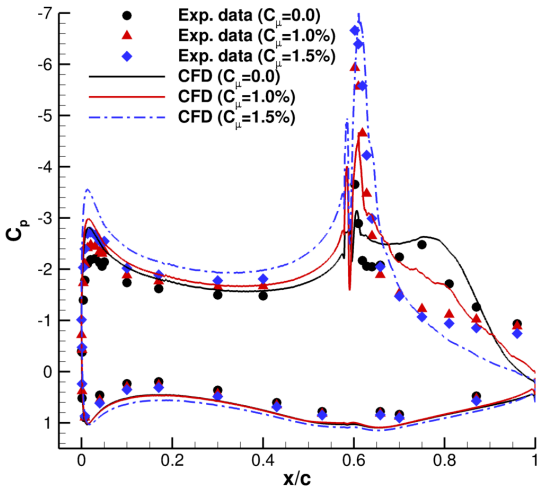
**(a) inboard,** $z/b = 40\%$
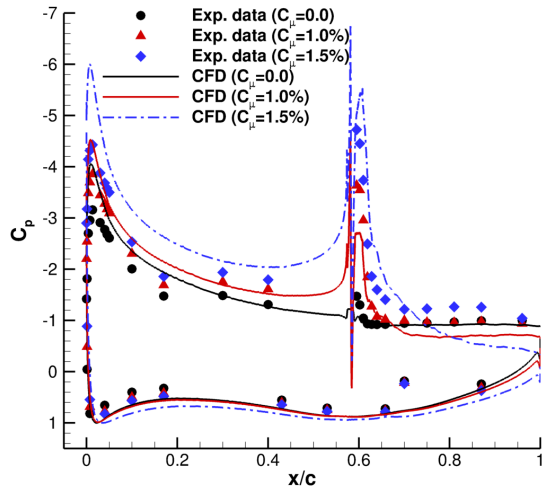


**(b) middle,** $z/b = 70\%$
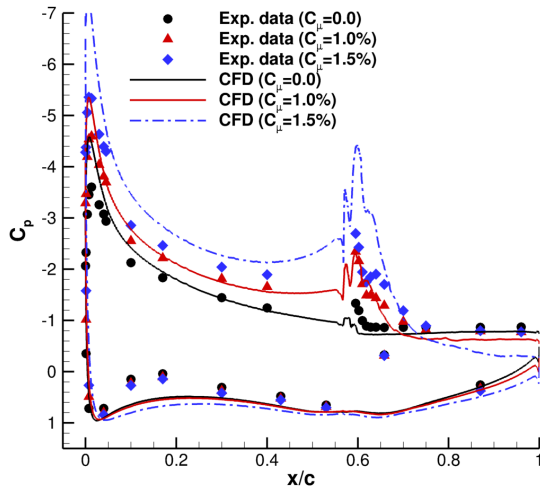


**(c) outboard,** $z/b = 89\%$

**Figure 9. Chordwise surface pressure comparisons: baseline case,** $\delta_R = 40°$, $\beta = 0°$.

American Institute of Aeronautics and Astronautics
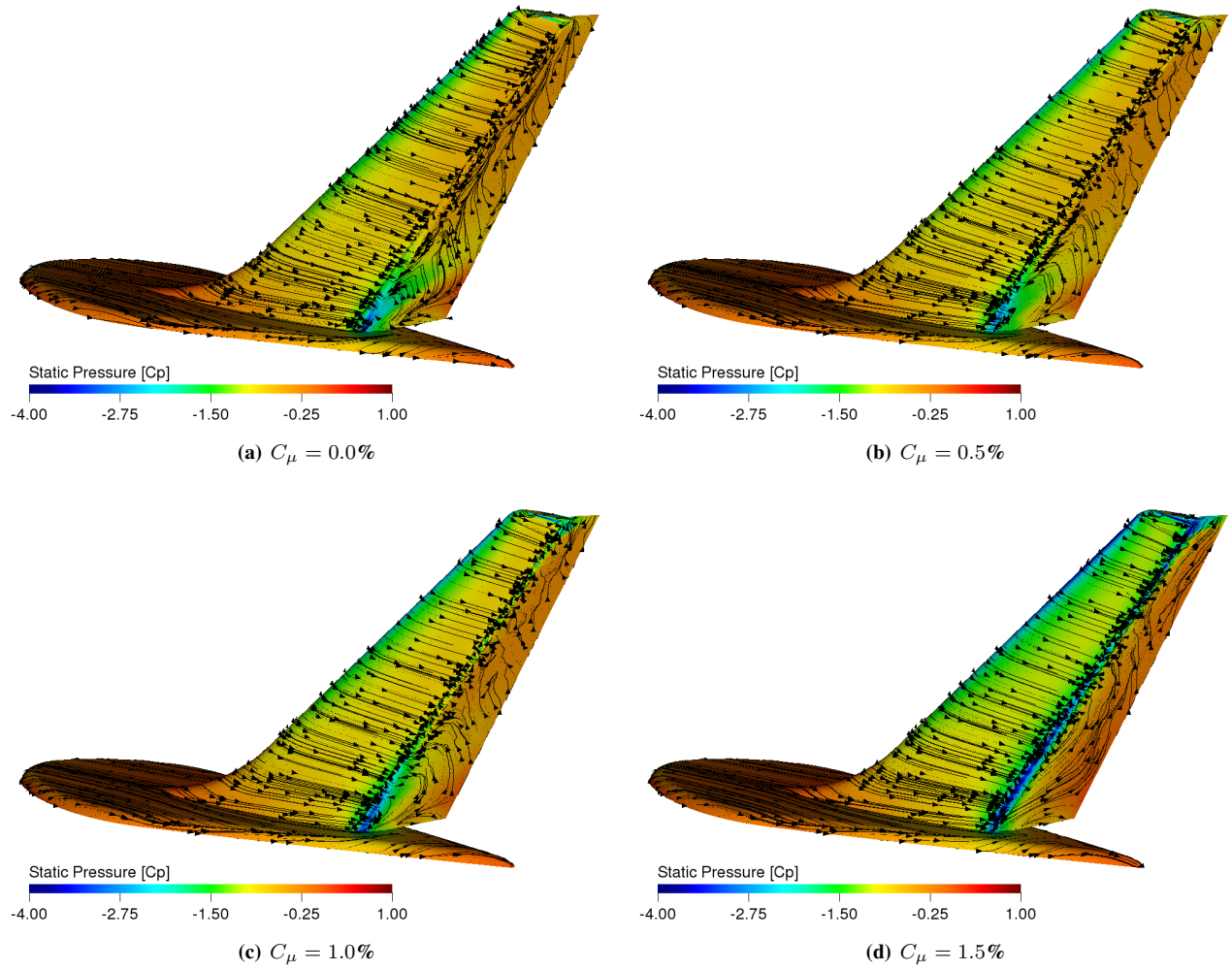
(a) $C_\mu = 0.0\%$

(b) $C_\mu = 0.5\%$

(c) $C_\mu = 1.0\%$

(d) $C_\mu = 1.5\%$

**Figure 10. Effect of actuation levels on simulated surface streamline patterns,** $\delta_R = 40°, \beta = 0°$.

American Institute of Aeronautics and Astronautics
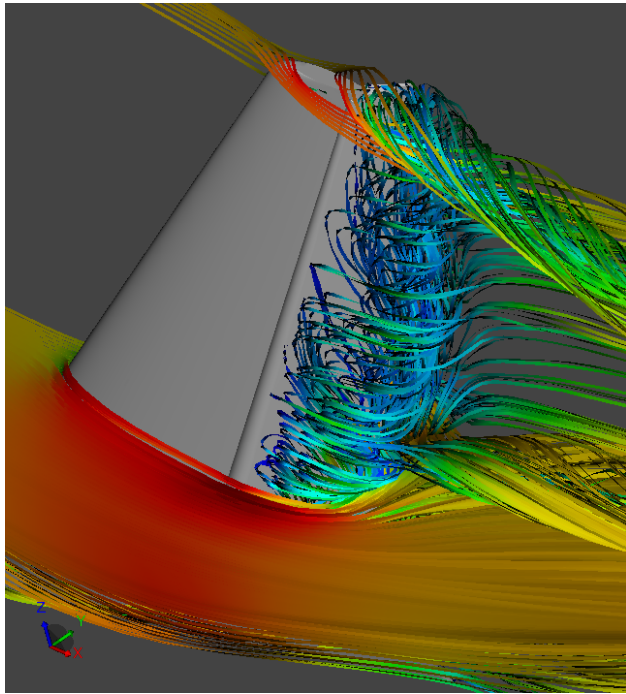
**(a)** $C_\mu = 0.0\%$
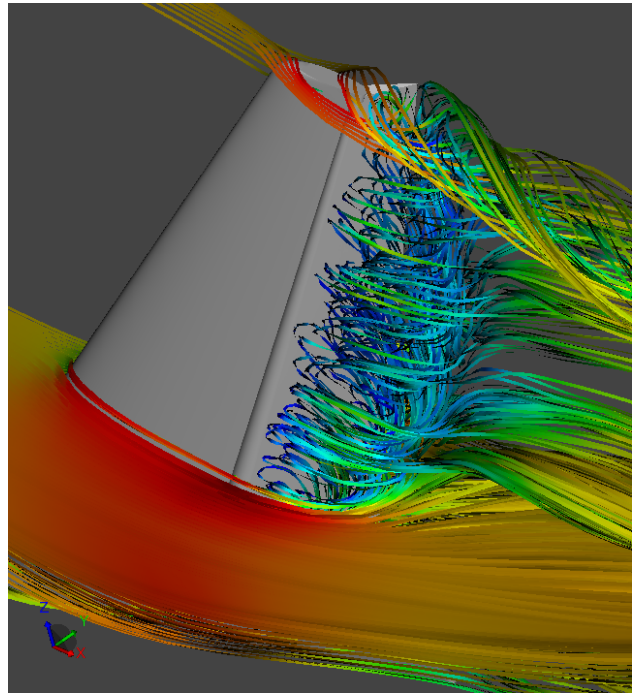
**(b)** $C_\mu = 0.5\%$
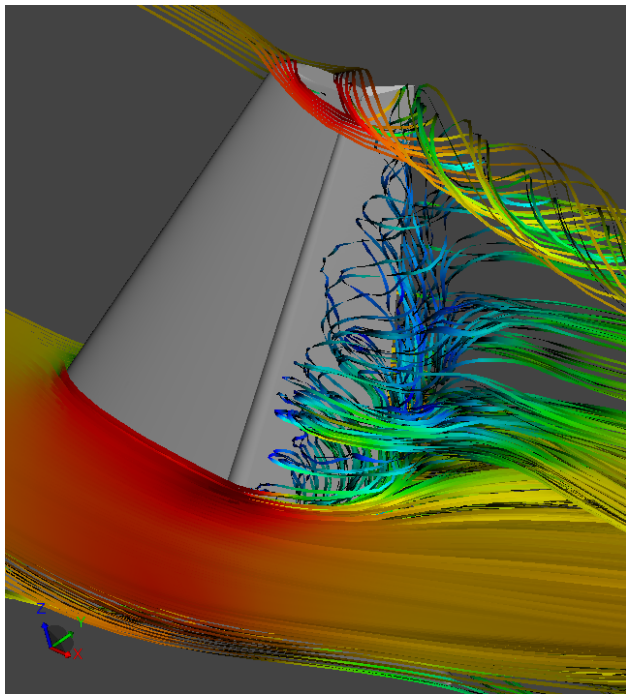
**(c)** $C_\mu = 1.0\%$
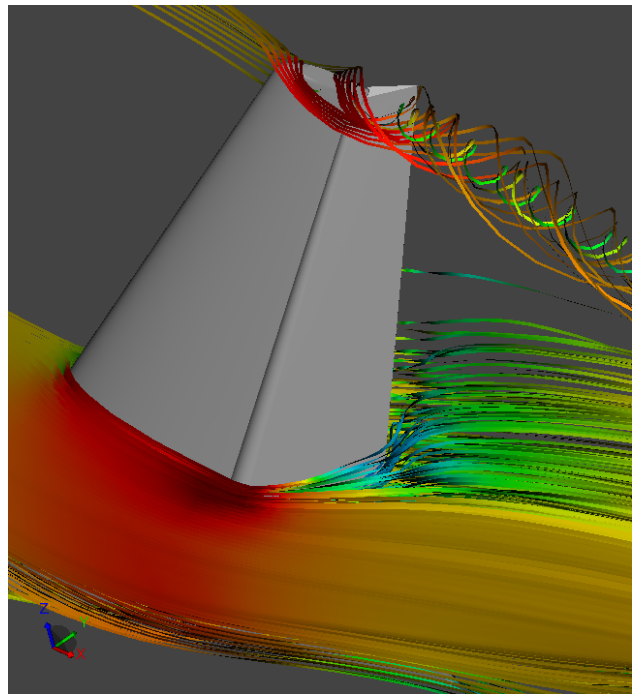
**(d)** $C_\mu = 1.5\%$

**Figure 11. Effect of actuation levels on simulated off-surface streamlines, $\delta_R = 40°$, $\beta = 0°$.**
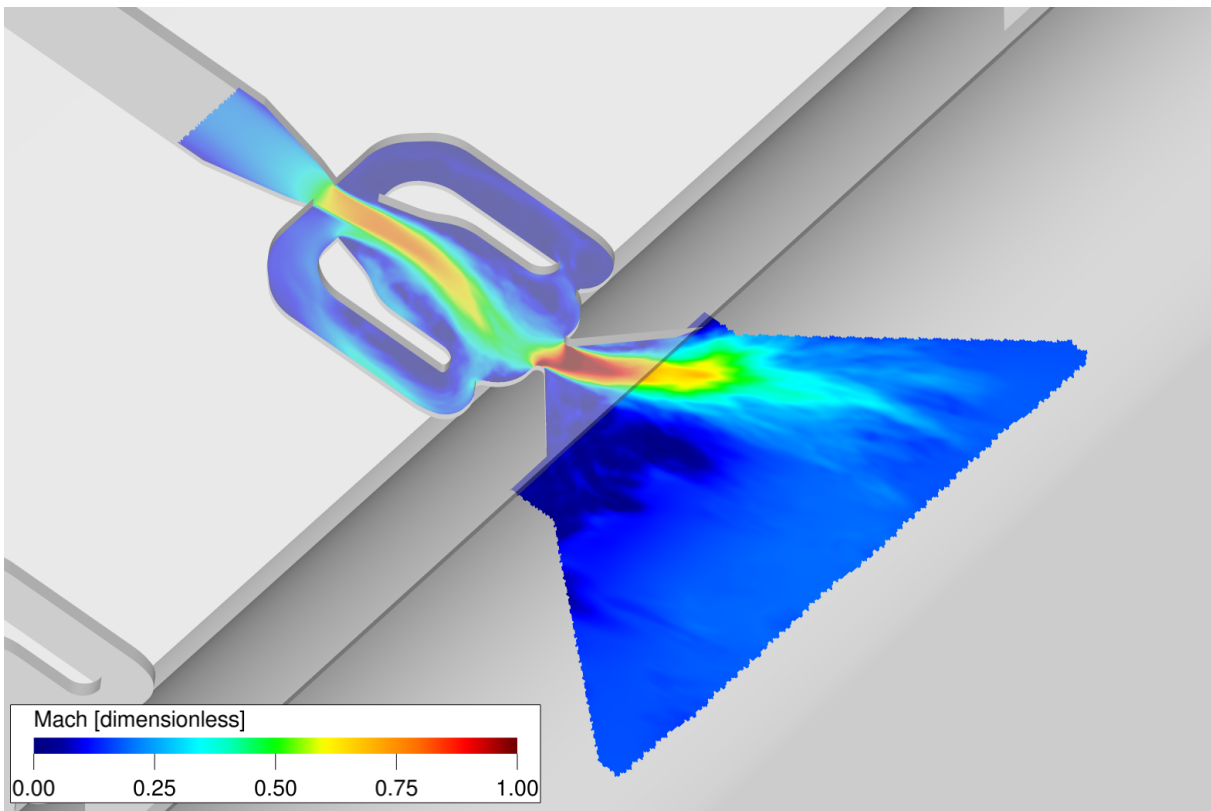
(a) Frame 1
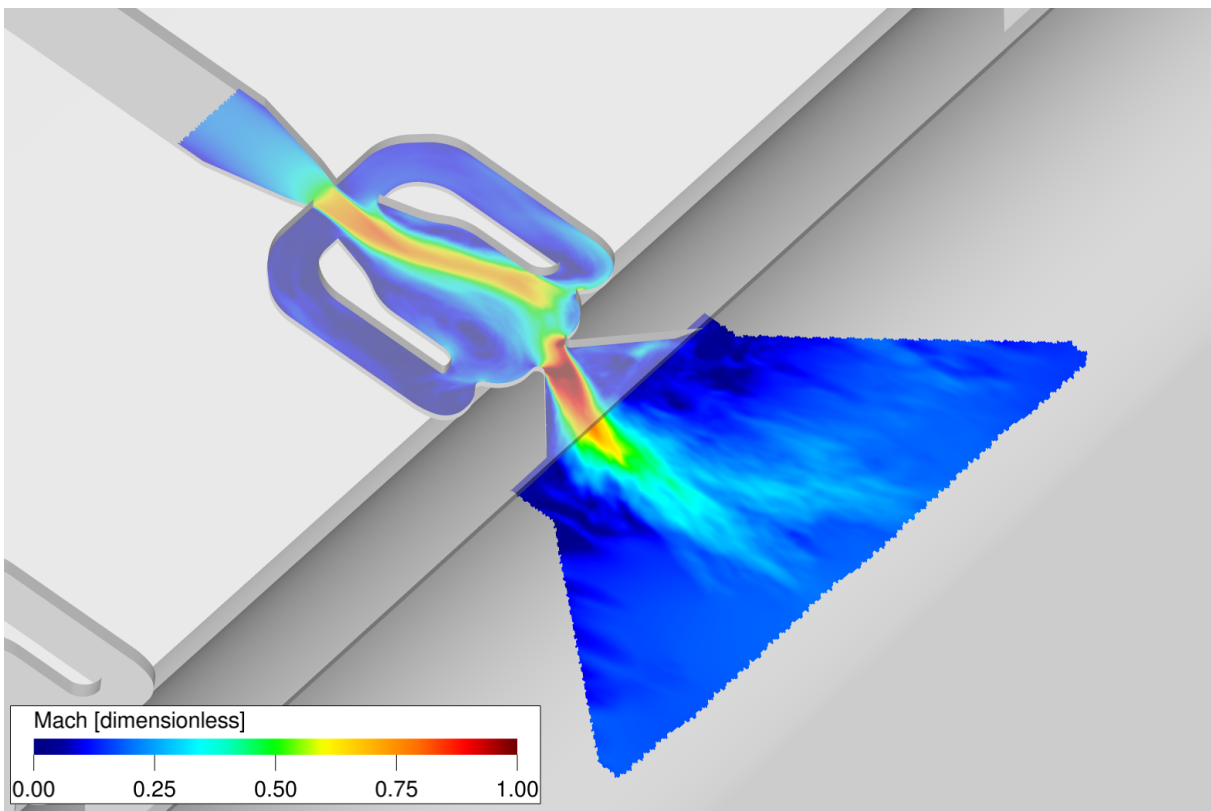


(b) Frame 2

Figure 12. Mach contours for middle actuator, $\delta_R = 40°, C_\mu = 1.5\%$.